RSC Advances

RSC Advances

www.rsc.org/advances

ROYAL SOCIETY OF CHEMISTRY

www.rsc.org/advances

Journal Name

Dynamic Article Links ▶

ARTICLE TYPE

Size-controlled synthesis of mesoporous Nb_2O_5 microspheres for dye sensitized solar cells

Xiujuan Jin, Chenliang Liu, Jing Xu, Qiufan Wang and Di Chen*

Mesoporous Nb_2O_5 microspheres assembled by nanoparticles are successfully synthesized through a simple solvothermal process and subsequently annealing treatment, free of any template or catalyst. By controlling the reactant $NbCl_5$ concentration, we could easily tune the diameter of the Nb_2O_5 spheres from 200 to 900 nm, which were also used to fabricate dye-sensitized solar cells. Studies found that dye-
10 sensitized solar cells based on Nb_2O_5 with the size of around 480nm shows the highest power conversion efficiency of 2.97% with a relatively high short current density (J_{sc}) of 6.8 mA cm^{-2} and an open circuit voltage (V_{oc}) of 0.738 V, which benefits from its higher specific surface area for adsorbing more dye molecules, superior light scattering capacity for boosting the light-harvesting efficiency, and modest electron transport property.

15 Introduction

Dye-sensitized solar cells (DSSCs) as a promising alternative to silicon-based cells have drawn intense attention due to their tunable optical properties, such as colour and transparency, minimal environmental impact, low cost, facile fabrication
20 process, short energy payback time, and comparable performance in most operating conditions.[1-4] The performance of DSSC, measured in terms of power conversion efficiency, depends closely on the light harvesting efficiency, the transport of the photoinjected electrons through the semiconductor electrode, and
25 the dynamics of interfacial losses resulting from the possible recombination of electrons with the electrolyte. Till now, much research has been conducted to enhance the efficiency of the DSSCs. With the main intention of improving the light harvesting efficiency, mesoporous spheres have been successfully
30 introduced as photoanodes fabricated from TiO_2 and attained excellent results in DSSCs.[5,6,7] The mesoporous spheres aggregated from nanoparticles with tunable porous structure, ensuring a large specific surface area, are beneficial to load dye. Meanwhile, the spheres with a proper submicrometer size are
35 suitable to be employed as light scattering layer to enhance optical absorption. Therefore, this structure is promising to function as dye adsorption layer as well as light scatterers layer to improve performance in DSSCs. Besides, porous structure and size would have an influence on elecron transport property. A
40 high power conversion efficiency of cells would be obtained only with the balance between light harvesting efficiency and the electron transport and recombination, by tuning the size and pores distribution of mesoporous spheres.

As a typical wide band gap metal oxide, TiO_2 has been widely
45 used in DSSCs photoanode and achieved more than 12% power conversion efficiency. Besides TiO_2, other semiconductor metal oxides such as ZnO, Nb_2O_5, SnO_2, $SrTiO_3$, Zn_2SnO_4, and other composites have also been investigated as potential alternatives to

TiO_2.[8-13] Among these, Nb_2O_5 could be a suitable candidate in
50 views of its wider band gap ranging between 3.2 and 4 eV, more negative conduction band edge position relative to TiO_2, comparable electron injection efficiency, as well as better chemical stability. It is expected that DSSCs assembled with Nb_2O_5 photoanode would attain a higher open circuit voltage and
55 power conversion efficiency.[14,15] To date, Nb_2O_5 with various nanostructures including nanoparticles, nanobelts, nanorods, nanowires, nanotubes, nanoporous networks and nanoforests have been synthesized by hydrothermal method, electrospinning technique, electrochemical anodization method and pulsed laser
60 deposition (PLD).[14-21] Nevertheless, to the best of our knowledge, mesoporous Nb_2O_5 microspheres from a mild hydrothermal process without the existance of the strong acid or alkaline environment were few reported.

Here, we reported a facile solvothermal method, free of any
65 template and catalyst to synthesize mesoporous Nb_2O_5 microspheres with tunable size ranging from 200-900 nm. The synthesized microspheres were characterized by SEM, TEM, SAED, XRD, FTIR and BET, respectively. The spheres based DSSCs with various sizes have also been studied. Results show
70 that Nb_2O_5 microspheres with diameter of around 480 nm display a best DSSCs performance when assembled into the photoanode.

Experiment details

All the reagents used in the experiment were as received without further purification.

75 1. Synthesis of mesoporous Nb_2O_5 microspheres

Firstly, different amounts of niobium (V) chloride ($NbCl_5$, Alfa, 99.9 % purity) were dissolved in ethanol (25 mL) in a 50 mL Teflon-lined stainless steel autoclave (0.3，0.42，0.5 g $NbCl_5$ for samples S1，S2，and S3，respectively). After stirring for
80 5min, the autoclave was sealed and heated to 200 °C for 24 h.

The white precipitates were collected, washed with deionized water and ethanol for several times and allowed to dry in air at 80 °C. Then the obtained precipitates were calcined at 550 °C for 2 h in air to obtain the mesoporous Nb_2O_5 beads.

2. Preparation of the DSSCs working electrodes

To prepare the photoanodes of DSSCs, the synthesized porous Nb_2O_5 beads, ethyl cellulose, and terpineol with a mass ratio of 1：5：4，respectively, were added into ethanol under stirring to form slurry. This mixture was then ultrasonicated to make it homogeneous by using an ultra-sonic horn for several minutes, and sequently evaporated by rotary-evaporator at 40 °C until a viscous paste was produced. The paste was screen-printed onto fluorine-doped tin oxide (FTO) coated glass with an active area of 0.196 cm^2. The resulting films were sintered at 550 °C for 1h, then soaked with an absolute ethanol solution containing 0.5 mM Ruthenizer 535 bis-TBA (N719 dye, Solaronix) for 24 h at room temperature.

After being washed with ethanol for several times, the sensitized working electrodes were assembled and sealed with the counter electrodes using a 25 μm thick Surlyn gasket to produce sandwich type cells. The counter electrodes were prepared by dropping the absolute ethanol solution containing 5 mM H_2PtCl_6 onto the FTO glass with subsequent heat treatment at 400 °C for 15 min under air. The electrolyte, 1.0 M 1, 2-dimethyl-3-propylimidazolium iodide (DMPII), 0.1 M LiI, 0.12 M I_2, and 0.5 M 4-TBP in methoxypropionitrile, was introduced into the cell via a vacuum filling method.

3. Characterization

Morphologies of the samples were observed by using a field emission scanning electron microscopy (SEM, FEI Sirion 200 and JEOL JSM 6700F) and high-resolution transmission electron microscopy (TEM) images and selected-area electron diffraction (SAED) patterns were taken with a Philips CM 200 FEG TEM. X-Ray diffraction (XRD, X'Pert PRO with Cu K α radiation) was used to verify crystal phase. FTIR analysis of the samples was performed using a VERTEX 70 FT-IR spectrometer. Nitrogen adsorption-desorption were measured by using a ASAP 2020 accelerated surface area and porosimetry system at -196 °C. Brunauer–Emmett–Teller (BET) method was used to calculate the specific surface area. The pore size distributions of the materials were derived from the adsorption branches of the isotherms based on the Barett-Joyner-Halenda (BJH) model. The Nb_2O_5 film thickness was measured using a profilometer (Dektak 150, Veeco Instruments Inc). The amount of dye loading was determined by desorbing the dye molecules from the sensitized photoanode films in 0.1 M NaOH ethanol solution and measuring the adsorption peak intensity of N719 at 515 nm with a spectrophotometer (Shimadzu UV-2550). Diffuse reflectance spectra of the films were recorded on a Shimadzu UV-2550 spectrophotometer equipped with an integrating sphere.

4. Measurements

The current–voltage characteristics were measured using a Keithley 2400 Source Metre under the illumination of simulated sunlight (100 mW cm^{-2}) provided by a solar simulator with an AM 1.5 G filter (Oriel, model 91192). Incident photon-to-current conversion efficiency (IPCE) as a function of wavelength was measured on the basis of a Newport Apex Monochromator illuminator (model 7010 4). Intensity modulated photovoltage spectroscopy (IMVS) and intensity modulated photocurrent spectroscopy (IMPS) measurements were carried out on a electrochemical workstation (Zahner, Zennium) with a frequency response analyzer under a diode laser light source with tunable intensity at 525 nm, which can provide both dc and ac components of the illumination. The modulated light intensity was 10 % or less than the base light intensity. The frequency range was set from 100 KHz to 0.1 Hz.

Results and Discussion
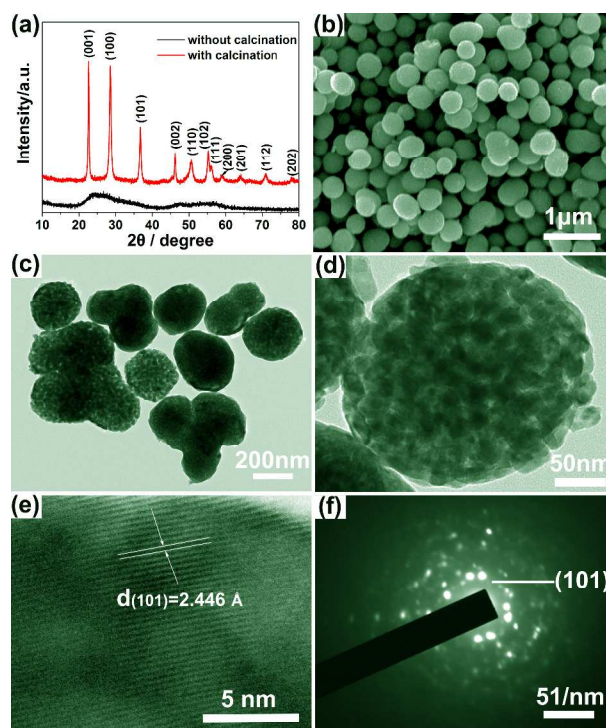
Figure 1. (a) XRD pattern, (b) SEM image, (c and d) TEM images, (e) HRTEM image and (f) SAED pattern of the Nb_2O_5 microspheres (S1).

Mesoporous Nb_2O_5 microspheres with various diameters were prepared from the facile solvothermal process and subsequent heating treatment. As an example, S1 synthesized with 0.3 g $NbCl_5$ dissolved in ethanol (25 mL) has been characterized. The XRD patterns of the synthesized Nb_2O_5 spheres and the precursors are shown in Fig. 1a. It reveals that the synthesized precursors are amorphous without obvious characteristic diffraction peaks. When calcined at 550 °C for 2h, high crystalline Nb_2O_5 samples were obtained. And all the peaks can be readily indexed to the hexagonal Nb_2O_5 with lattice parameters of a=3.607 Å, c=3.925 Å (JCPDS no. 7-61) and without impurity peaks detected. Fig. 1b shows the SEM image of the precursors. It is observed that, spherical precursors with diameter range from 200-300 nm were firstly synthesized from the solvothermal process. After calcined, spherical Nb_2O_5 samples with similar size were obtained as shown in Figure 1c and 1d. TEM images clearly show that spherical Nb_2O_5 samples are porous and composed of nanocrystals (dozens of nanometers). Furthermore, Figure 1e shows the HRTEM image of sample, the clear crystal fringes with a lattice spacing of d=2.446 Å can be

ascribed to (101) planes of hexagonal Nb_2O_5, corresponding well with XRD analysis. The concentric circles composed of bright dots in the SAED pattern (Fig. 1f) confirms the polycrystalline structure of the Nb_2O_5 spheres.
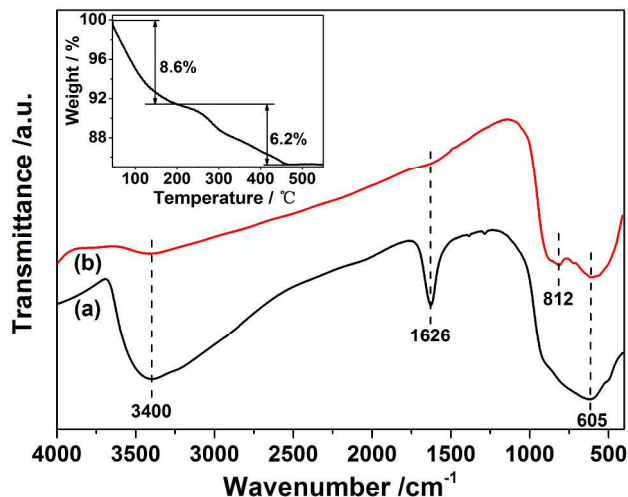
Figure 2. FTIR spectra of the precursor S1 (a) and calcined mesoporous Nb_2O_5 beads at 550 °C for 2h. The inset of TG curve of the precursor S1.

The structure transformation of spheres caused by the calcination is also confirmed by the Fourier transform infrared spectroscopy (FTIR) and thermogravimetric analysis (TGA), respectively. FTIR spectrum of the as-synthesized precursor as shown in Fig. 2a clearly exhibits a broad absorption peak at ~3400 cm^{-1}, which could be associated with the asymmetric and symmetric stretching vibrations of the -OH group of absorbed water molecules and the surface hydroxyls as well as the ethylene glycol units. And a sharp peak at 1626 cm^{-1} can also be assigned to the bending vibrations of the water molecules.[22, 23, 24] A broad band centered at 605 cm^{-1} can be assigned to symmetric stretching of the niobium polyhedral.[25] After calcination treatment, all peaks disappeared except for the Nb-O band at 605 cm^{-1} in Fig. 2b. Besides, a new peak at 812 cm^{-1} can be found, which marks the formation of hexagonal structure. The TG curve (inset of Fig.2) recorded in air indicates a two-step pattern for weight loss of the precursor. From room temperature to 110 °C, the weight loss of 5% corresponds to desorption of physically adsorbed water molecules. The weight loss of 10% from 110 to 450 °C is associated with the removal of ethylene glycol units

and the degradation of organic groups contained in the precursor particles.[23] These observations confirm the removal of OH group and the formation of Nb_2O_5 crystalline phase from the amorphous structure at 550 °C. And higher calcination temperature would lead to a phase transformation and an reduction in BET. Based on the above analysis, the formation mechanism of the mesoporous Nb_2O_5 microspheres could be concluded as following: First is the hydrolysis of $NbCl_5$ in ethanol and the formation of amorphous particles in the solvothermal process. Then, with the increasing of reaction time, particles aggregated each other into microshperes resulting in the formation of amorphous precursors. Finally, the precursors were further transferred into crystalline phase with annealing treatment. At the same time, organic groups were removed and mesoporous structures were left. The possible formantion process of mesoporous Nb_2O_5 spheres is schematically illustrated in Fig. 3.

During the preparation process, it was found that the initial reactant concentration had an obvious influence on the size and microstructure of the samples. As shown in Fig. 4a-4c, by varying the amount of $NbCl_5$ from 0.3 to 0.5g, three spherical precursors with the diameters ranging from 200 to 900 nm were prepared without changing the current procedure. Fig.4d, 4f, 4h further show high SEM images of the precursors, respectively. After calcined, mesoporous spheres with the diameters of about 220 nm, 480 nm and 900 nm were synthesized and the corresponding samples were assigned to S1 (Fig. 4e), S2 (Fig. 4g), and S3 (Fig. 4i), respectively. These synthesized products consisting of a large quantity of nanoparticles show mesoporous structure, which are quite different from the precursors. XRD patterns shown in Fig. S1a-d further confirm that amorphous niobium glycolates have been fully transformed into hexagonal Nb_2O_5. Obviously, the size of spheres increases with the increase of the $NbCl_5$ concentration, which can be well explained by the mechanism of nucleation and growth. As some literatures reported, [26-29] with the increase of reactant concentration, the hydrolysis rate accelerated resulting in the higher rate of nucleation. At the same time, the growth rate of crystallite is suppressed at certain degree leading to the formation of particles with smaller size. Then the aggregation rate of particles increased and larger microspheres were prepared with the increasing of reactant concentration.
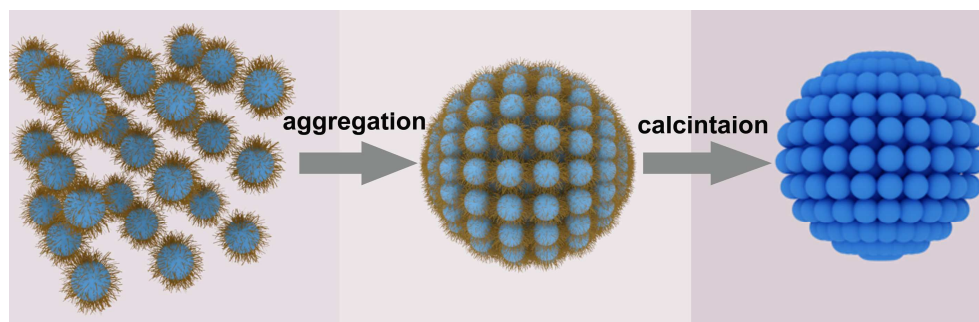
Figure 3. Schematic illustration of the formation mechanism of the mesoporous Nb_2O_5 microspheres
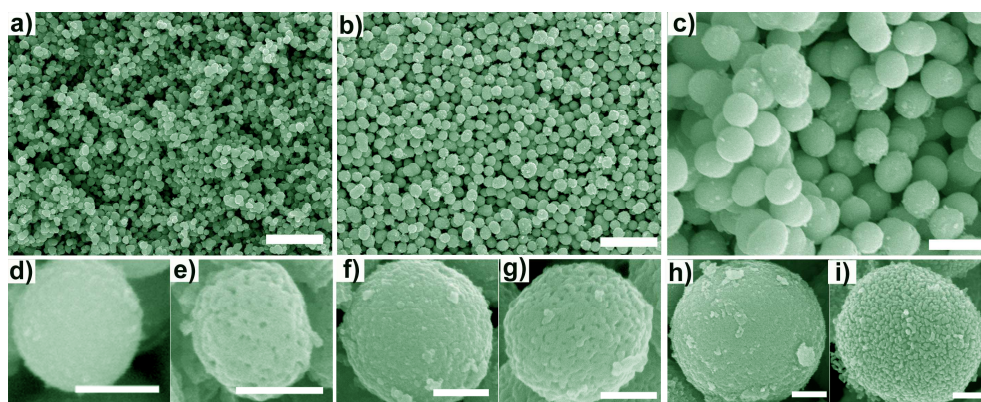
Figure 4. SEM images of the niobium glycolate precursors S1 (a, d), S2 (b, f), S3 (c, h) prepared through controlled hydrolysis of $NbCl_5$ in ethanol with 0.3, 0.42, 0.5 g $NbCl_5$, and Nb_2O_5 products S1 (e), S2 (g), S3 (i) after calcination treatment at 550 °C for 2h. Note: (a-c) scale bar: 2μm，(d-i) scale bar: 200nm.
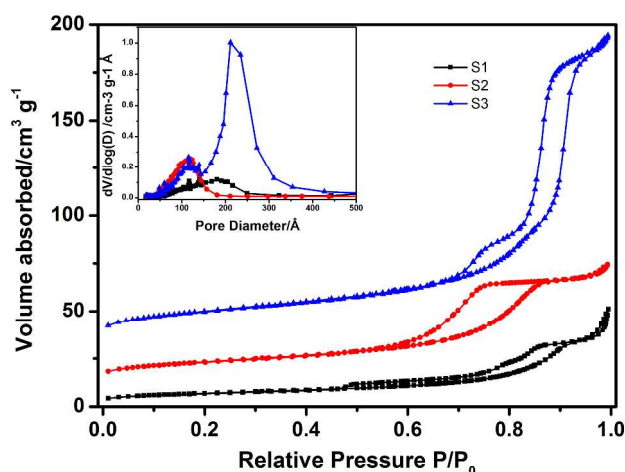
Figure 5. Nitrogen adsorption and desorption isotherms of the calcined mesoporous Nb_2O_5 beads (sample S1，S2，and S3). The isotherms of samples S2 and S3 are shifted by 10 and 30 cm^3 g^{-1} (STP), respectively. Inset shows the corresponding pore diameter distribution.

Table 1. Characterizaion and DSSCs photovoltaic performance parameters of three samples measured under AM 1.5 full sunlight illumination (100 mW cm^{-2})

Devics	V_{oc} (V)	J_{sc} (mA cm^{-2})	FF (%)	η (%)	Thickness (μm)	BET (m^2 g^{-1})
S1	0.754	4.74	67.9	2.43	8	23.3
S2	0.738	6.81	58.9	2.97	8.5	44.9
S3	0.721	5.01	52.4	1.89	7.5	67.7

The specific surface areas and porous nature of three as-prepared mesoporous Nb_2O_5 microspheres were further investigated by nitrogen adsorption-desorption measurements, as shown in Fig. 5. Type IV isotherms with a substantial hysteresis loop in the P/P_0 range above 0.6 indicate the mesoporous structure of samples.[30, 31] Table 1 further summarized the tendency for the specific areas of samples enlarging as a function of reactant concentration. The specific areas of S1，S2，S3 are 23.3 m^2 g^{-1}, 44.9 m^2 g^{-1} and 67.7 m^2 g^{-1}, respectively. In general, a smaller size would result in a bigger BET surface area. Among three samples, sample S3 with the largest diameter shows the highest BET surface area, which is owing to its mesoporous structure. For sample S3, typical isotherm with two major

capillary condensation steps at relative pressure P/P_0 ranges 0.75-0.85 and 0.85-0.95 were observed, which also indicated the characteristic of hierarchical porous structure.[32, 33] Moreover, the pore size distribution curve (inset in Fig. 5) shows that the primary and secondary pore diameters are centered at 12 and 21 nm, respectively, indicating that the materials have unique hierarchical porous structures on at least two levels, and the majority of the available surface area is due to the presence of the mesopore at 21 nm. With the interesting mesoporous structure, the as-synthesized Nb_2O_5 spheres are promising to function as dye adsorption layer as well as light scatterers layer to improve performance in DSSCs.
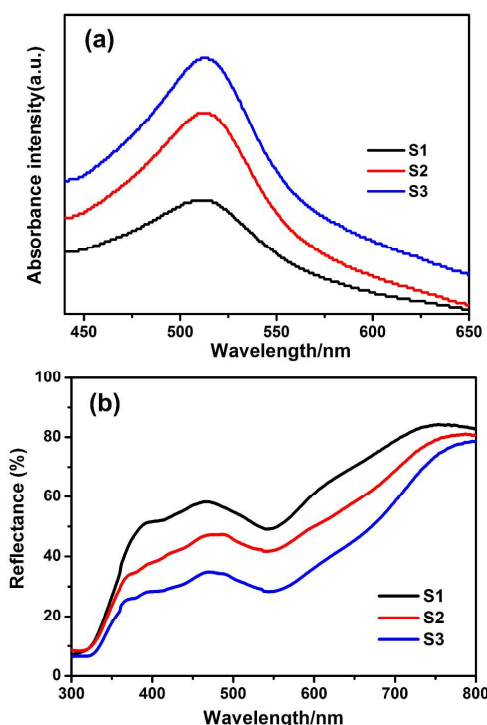
Figure 6. (a) UV-vis absorption spectra of desorbed dye molecular from the sensitized photoanode films in NaOH ethanol solution; (b) Diffused reflectance spectra of the three sensitized photoanode films.

To investigate the potential applications of the mesoporous Nb_2O_5 microspheres in DSSCs, Nb_2O_5 films as working

electrodes were prepared with various sizes using screen-printing technique. The films were subsequently annealed at 500 °C for 30 min in air to improve the contact between the microspheres and the FTO substrate and remove organic compounds added in
[5] paste. Then, as-prepared electrodes were sensitized with 0.5 mM N719 dye for 24 h. The amount of dye loading was determined by desorbing the dye molecules from the sensitized photoanode films in 0.1 M NaOH ethanol solution and measuring the adsorption spectra as shown in Fig. 6a. Obviously, the adsorbing
[10] capacity of Nb_2O_5 microspheres increased with the increased size, which is agreed well with the obtained specific surface area calculated from the BET analysis. The diffuse reflectance spectra of sensitized photoanode films with N719 were also brought (Fig. 6b). The reflectance of the sensitized films were drastically
[15] reduced at about 540 nm caused by the dye adsorption. Moreover, a red shift of about 25 nm were distinctively observed relative to the maximum absorption peak (~515 nm) of N719 dye (Fig. 6a), which were owed to the efficient light scattering of the microspheres. Similar phenomena were also observed by Park et
[20] al.[34] Accordingly, Nb_2O_5 microspheres with larger BET surface area exhibit a higher dye adsorption ability, leading to an enhancemt in the absorption of solar light. Thus, together with the efficient light scattering, the microspheres would yield an improvement in the light harvesting efficiency associated to
[25] photocurrent.
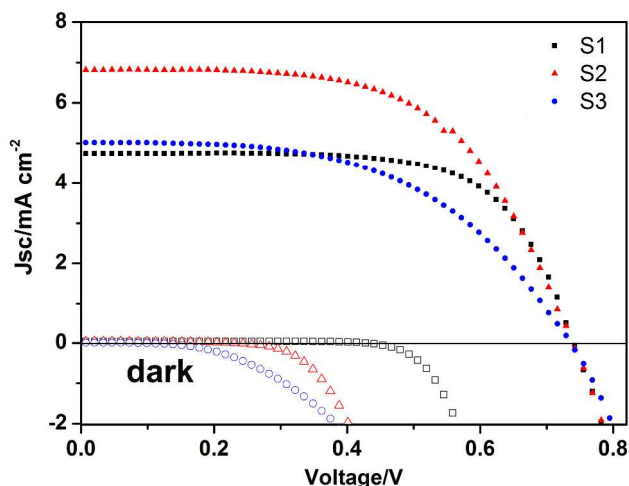
Figure 7. Current density-voltage (*J-V*) characteristics curves of DSSCs fabricated from three samples under AM 1.5 simulated sunlight with a power density of 100 mW cm^{-2} (solid marks) and dark (hollow marks).

[30] Subsequently, the photovoltaic properties of three different photoanodes were tested. The photocurrent density-voltage (*J-V*) characteristics were measured under standard AM 1.5 illumination with a power density of 100 mW cm^{-2}. The corresponding results are shown in Fig. 7, and the detailed
[35] photovoltaic parameters are summarized in Table 1. The fill factor (*FF*) and power conversion efficiency (*η*) were determined by the following equations.

$$FF = V_m \cdot J_m / V_{oc} \cdot J_{sc} \qquad (1)$$

$$\eta = V_{oc} \cdot J_{sc} \cdot FF / P_{in} \qquad (2)$$

[40] where V_m and J_m are the voltage and current density at maximum

power output; V_{oc} and J_{sc} are the open-circuit voltage and short-circuit current density, respectively; and P_{in} is the incident light power density. The film thickness of of devices was optimized in our case. Based on above discussed, although S3 exhibited the
[45] highest dye loading ability, the best device performance with the highest efficiency of 2.97% was achieved by using S2 as photoanode. And the corresponding short current density (J_{sc}) and open circuit voltage (V_{oc}) were 6.8 mA cm^{-2} and 0.738 V, respectively. It was also noted that, with the increase in size, the
[50] V_{oc} decreased from 0.75 to 0.72 V. According to the literatures,[35-38] the charge recombination sites would lead to a decrease of V_{oc}, which mainly takes place at nanocrystalline/redox electrolyte interfaces. The injected conduction band electrons may recombine with oxidized dye moleculars on the interfaces or with
[55] tri-iodide and poly-iodide redox species in the electrolyte. In this case, firstly, a big dye adsorption capacity causing the increase of excited electron concentration would accelerate recombination. Secondly, the bigger microspheres containing more nanoparticles bring more interfaces, which provide a site for charge
[60] recombination. The recombination of charges were also characterized by dark current-voltage characteristics curves as shown in Fig. 7 (hollow marks). The onset of dark current occurred at highest potential for S1 and lowest for S3, indicating the low recombination loss in S1, which were agreement with the
[65] V_{oc} value. Besides, the relatively low photocurrent density of S3 with the most dye loading ability could be also explained by the enlarged interface recombination. Thus, with balancing between charge recombination and photo absorption, S2 obtained the highest overall photoelectric conversion efficiency of 2.97 % in
[70] three samples.
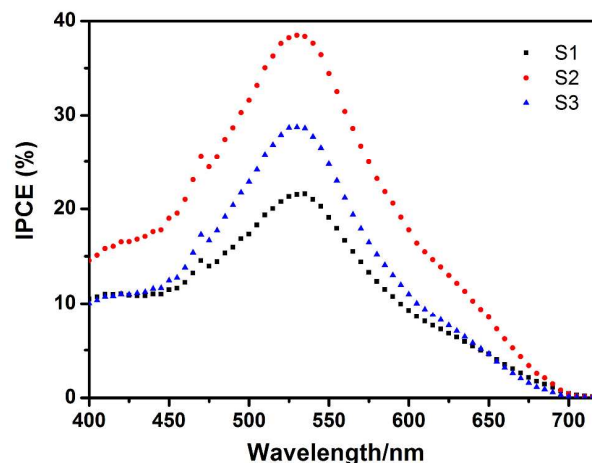
Figure 8. Incident photon to current conversion efficiency (IPCE) curves of the Nb_2O_5 electrodes prepared from obtained beads with different sizes.

The differences in photocurrent density of these three solar
[75] cells were further investigated by measuring the incident-photon-to-collected-electron efficiency (IPCE) spectra as a function of wavelength, and the results are exhibited in Fig. 8. The photocurrent density J_{sc} and IPCE under each wavelength of radiation can be expressed by the following equations:[39, 40, 41]

[80] $$J_{sc}(\lambda) = q\eta_{IPCE}(\lambda) I_0 \qquad (3)$$

$$\eta_{IPCE}(\lambda) = \eta_{lh}(\lambda)\eta_{inj}(\lambda)\eta_{cc}(\lambda) \qquad (4)$$

where q is the elementary charge, η_{IPCE} (λ) is the quantum efficiency under each light wavelength, I_0 is the illuminated light intensity, η_{lh} is the light-harvesting efficiency of a cell, η_{inj} is the charge-injection efficiency and η_{cc} is the charge collection efficiency. The whole short circuit current can be obtained by integrating Eq (3). High quantum efficiency means a high short current density. In our case, S2 exhibited a highest IPCE value, and S1 lowest, which matched well with the results of short current density. The product of η_{lh}, η_{inj}, and η_{cc} is commonly referred to the incident photon-to-current conversion efficiency as expressed in Eq (4). Of the three parameters, η_{lh} is mainly determined by the amount of adsorbed dye, and η_{inj} values of adsorbed N719 on the films can be assumed to be the same. So the factor limiting the performance of S3 should be the low η_{cc} largely determined by the competition between recombination and charge collection.
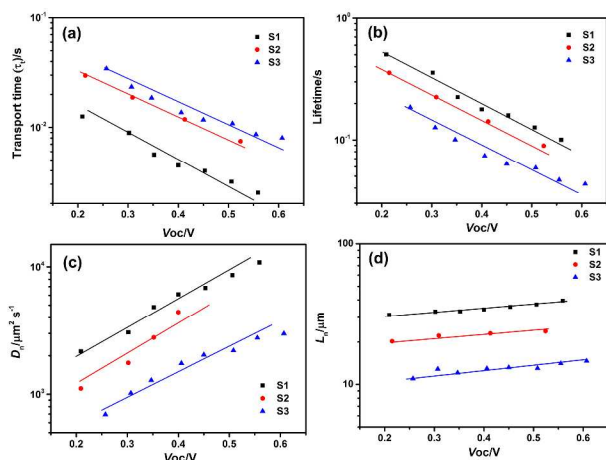
Figure 9. Electron transport and recombination kinetics determined from IMPS/IMVS. (a) Transport time. (b) Lifetime. (c) Electron diffusion coefficient. (d) Effective diffusion length of the three DSSCs fabricated from S1，S2，and S3.

To understand the electron transport and interfacial charge recombination process in these devices, intensity modulated photocurrent/photovoltage spectroscopy (IMPS/IMVS) were performed. The electron transport is determined by diffusion, the lifetime of photon-generated electrons is determined by back reaction with oxidized species in the electrolyte, and the electron diffusion length is determined by the competition between electron transport and back reaction.[42, 43, 44] In these studies, we used a diode laser light source with tunable intensity at 525 nm, a wavelength close to the absorption peak of N719 dye. Fig. 9 shows the plots of electron transport time (τ_t), electron lifetime (τ_n), electron diffusion length (L_n) and diffusion coefficient (D_n) as a function of open-circuit voltage (V_{oc}) obtained at different light intensities, respectively. The electron transport time (τ_t) can be calculated from the IMPS response by $\tau_t = 1/(2\pi f_{minIMPS})$ at short circuit. Correspondingly, the electron lifetime (τ_n) can be obtained from IMVS by $\tau_n = 1/(2\pi f_{minIMVS})$ at open circuit.[45] The electron diffusion coefficient (D_n) and electron diffusion length (L_n) are determined from the following expressions: $D_n = d^2/2.35\tau_t$ and $L_n = (D_n\tau_n)^{1/2}$, respectively, where d is the film thickness, and the factor of 2.35 arises from the geometry of the diffusion problem.[46, 47] In Fig. 9a and 9b, the τ_t and τ_n of the three cells decrease with the more negative V_{oc}. The slower transport rate

and larger recombination rate with the increasing microspheres size indicate that trap sites and recombination centers in the microspheres aggregated from nanoparticles increased. The shortened electron lifetime also explained the decreased open circuit voltage from 0.74 V to 0.72 V. In addition, the electron diffusion coefficient and effective diffusion length of the cells were shown in Fig. 9c and 9d, respectively. Obviously, S1 possesses the quickest diffusion rate and the longest effective diffusion length in three cells. And the D_n and L_n curves of S2 only slightly lower than S1, also shows a good transport property. In contrast, S3 composed of more nanoparticles would have more boundaries and defects, in which the electron could be trapped to some extent during the process of transport, leading to a terrible performance. After considering all the factors above, the higher short circuit current density and power conversion efficiency of S2 can be mainly attributed to the higher specific surface area for adsorbing more dye molecules and superior light scattering capacity for facilitating the light harvesting efficiency compared with S1 as well as modest electron transport rate and recombination time when compared with S3. Hence, a highest photoelectric conversion efficiency of 2.97 % was successfully achieved for S2.

Conclusion

In summary, by controlling the reactant concentrations, mesoporous Nb_2O_5 microspheres with various diameters from 200-900 nm were prepared from a mild solution route and post treatment process. Furthermore, the DSSCs based on these Nb_2O_5 beads with different sizes have also been studied. We received the highest power conversion efficiency of 2.97% by using Nb_2O_5 with diameter of around 480 nm (S2) as photoanode, with a highest short current density (J_{sc}) of 6.8 mA cm^{-2} and a relatively high open circuit voltage (V_{oc}) of 0.738 V. The investigations of IMPS and IMVS reveal that the electron transport and recombination for S2 are slightly inferior to the S1，but obviously superior to the S3 due to affection of the trapping sites and recombination centres. However, high specific surface area and suitable pores, big dye adsorbing amount and light scattering capacity enhanced the light-harvesting efficiency, which is responsible for the improvement of photocurrent. After trading off between the electron transport property and light harvesting efficiency, S2 achieved the highest power conversion efficiency. The results indicate that the synthesized mesoporous Nb_2O_5 microspheres with appropriate size and pores distribution are efficient photoanode for the dye-sensitized solar cells. Compared to TiO_2 as photoanode, the relatively low efficiency might have mainly been attributed to the poor dye loading owing to mismatch between anode materials and dye. Thus, we believed that with proper optimization, the performance of Nb_2O_5 based DSSCs should be further improved.

Micro-Fabrication and Characterization (CMFC) of WNLO for the samples measurements.

Notes and references

Wuhan National Laboratory for Optoelectronics and School of Optical and Electronic Information, Huazhong University of Science and Technology, Wuhan 430074, China. Fax: 86 27 87792225; E-mail: dichen@mail.hust.edu.cn

1　B. O'Regan, and M. Gräetzel, *Nature*, 1991, **353**, 737.

2　M. Gräetzel, *Nature*, 2001, **414**, 338.

3　Z. R. Wang, H. Wang, B. Liu, W. Qiu, J. Zhang, S. Ran, H. Huang, J. Xu, H. Han, D. Chen and G. Z. Shen, *ACS Nano*, 2011, **5**, 8412.

4　A. Hagfeldt, G. Boschloo, L. Sun, L. Kloo, and H. Pettersson, *Chem. Rev.* 2010, **110**, 6595.

5　K. Y. Yan, Y. C. Qiu, W. Chen, M. Zhang, and Shihe Yang. *Energy Environ. Sci.*, 2011, **4**, 2168.

6　F. Z. Huang, D. H. Chen, X. L. Zhang, R. A. Caruso, and Y. B. Cheng. *Adv. Funct. Mater.* 2010, **20**, 1301.

7　T. G. Deepak, G. S. Anjusree, S. Thomas, T. A. Arun, S. V. Nair and A. S. Nair, *RSC Adv*, 2014, **4**, 17615.

8　A. Yella, H. W. Lee, H. N. Tsao, C. Yi, A. K. Handiran, M. K. Nazeeruddin, E. W. G. Diau, C. Y. Yeh, S. M. Zakeeruddin, and M. Grätzel, *Science*, 2011, **334**, 629.
.

9　J. Qian, P. Liu, Y. Xiao, Y. Jiang, Y. Cao, X. Ai, and H. Yang, *Adv. Mater.* 2009, **21**, 3663.

10　J. –H. Lee, N. –G. Park, and Y. –J. Shin, Sol. *Energy Mater. Sol. Cells.* 2010, **95**, 179.

11　F. Lenzmann, J. Krueger, S. Burnside, K. Brooks, M. Gräetzel, D. Gal, S. Ruehle, and D. Cahen, *J. Phys. Chem. B*. 2001, **105**, 6347.

12　R. Jose, V. Thavasi, and S. Ramakrishna, *J. Am. Ceram. Soc.* 2009, **92**, 289.

13　S. G. Chen, S. Chappel, Y. Diamant, and A. Zaban, *Chem. Mater.* 2001, **13**, 4692.

14　P. Guo, and M. A. Aegerter. *Thin solid films*. 1999, **351**, 290.

15　A. L. Viet, R. Jose, M. V. Reddy, B. V. R. Chowdari, and S. Ramakrishna. *J. Phys. Chem. C*. 2010, **114**, 21795.

16　C. L. Yan, and D. F. Xue. *Adv. Mater.* 2008, **20**, 1055.

17　B. Varghese, S. C. Haur, and C. T. Lim. *J. Phys. Chem. C*. 2008, **112**, 10008.

18　X. S. Fang, L. F. Hu, K. F. Huo, B. Gao, L. J. Zhao, M. Y. Liao, P. K.. Chu, Y. Bando, and D. Golberg. *Adv. Funct. Mater.* 2011, **21**, 3907.

19　H. M. Zhang, Y. Wang, D. J. Yang, Y. B. Li, H. W. Liu, P. Liu, B. J. Wood, and H. J. Zhao. *Adv. Mater.* 2012, **24**, 1598.

20　J. Z. Ou, R. A. Rani, M. H. Ham, M. R. Field, Y. Zhang, H. D. Zheng, P. Reece, S. Zhuiykov, S. Sriram, M. Bhaskaran, R. B. Kaner, and K. Kalantar-zadeh. . *ACSNANO*. 2012, **6**, 4045.

21　R. Ghosh, M. K. Brennaman, T. Uher, M. R. Ok, E. T. Samulski, L. E. McNeil, T. J. Meyer, and R. Lopez. *ACS Appl. Mater. Interfaces.* 2011, **3**, 3929.

22　X. C. Jiang, T. Herricks, and Y. N. Xia. *Adv. Mater.* 2003, **15**, 1205.

23　S. Q. Shang, X. L. Jiao, and D. R. Chen. *ACS Appl. Mater. Interfaces.* 2012, **4**, 860.

24　X. F. Chen, X. C. Wang and X. Z. Fu. *Energy Environ. Sci.*, 2009, **2**, 872.

25　V. S. Braga, J. A. Dias, S. C. L.Dias, and J. L. de Macedo. *Chem. Mater.* 2005, **17**, 690.

26　J. Kim, Y. Rheem, B. Yoo, Y. Chong, K. N. Bozhilov, D. Kim, M. J. Sadowsky, H. G. Hur, and N. V. Myung. *Acta Biomaterialia*. 2010, **6**, 2681.

27　J. Q. Hu, Z. H. Wen, Q. Wang, X. Yao, Q. Zhang, J. H. Zhou, and J. H. Li. *J. Phys. Chem. B*. 2006, **110**, 24305.

28　J. L. Hu, H. S. Qian, Y. Hu, Z. Q. Li, G. X. Tong, T. K. Ying, P. J.Gong, S. Y. Hao, H. B. Zhang and L. C. Li. *CrystEngComm*. 2012, **14**, 7118.

29　H. E. Wang, L. X. Zheng, C. P. Liu, Y. K. Liu, C. Y. Luan, H. Cheng, Y. Y. Li, L. Martinu, J. A. Zapien, and I. Bello. *J. Phys. Chem. C.* 2011, **115**, 10419.

30　J. Wang, Y. K. Zhou, Y. Y. Hu, R. O'Hayre, and Z. P. Shao. *J. Phys. Chem. C.* 2011, **115**, 2529.

31　Q. F. Wang, B. Liu, X. F. Wang, S. H. Ran, L. M.Wang, D. Chen and G. Z. Shen. *J. Mater. Chem.*, 2012, **22**, 21647.

32　M. D. Ye, C. Chen, M. Q. Lv, D. J. Zheng, W. X. Guo, and C. J. Lin. *Nanoscale.* 2013, **5**, 6577.

33　Y. Wang, J. He, J. W. Chen, L. B. Ren, B. W. Jiang, and J. Zhao. *ACS Appl. Mater. Interfaces*. 2012, **4**, 2735.

34　Y. C. Park, Y. J. Chang, B. G. Kum, E. H. Kong, J. Y. Son, Y. S. Kwon, T. Park and H. M. Jang. *J. Mater. Chem.*, 2011, **21**, 9582.

35　J. B. Xia, N. Masaki, K. J. Jiang, and S.Yanagida. *Chem. Commun.*, 2007, 138.

36　M. Grätzel. *Prog. Photovolt. Res. Appl.*, 2000, **8**,171.

37　S. Ito, P. Liska, P. Comte, R. Charvet, P. Péchy, U. Bach, L. Schmidt-Mende, S. M. Zakeeruddin, A. Kay, M. K.. Nazeeruddin and M. Grätzel. *Chem. Commun.*, 2005, 4351.

38　G. L. Shang, J. H. Wu, S. Tang, M. L. Huang, Z. Lan, Y. Li, J. C. Zhao, and X. P. Zhang. *J. Mater. Chem.* 2012. **22**. 25335.

39　Z. R. Wang, S. H. Ran, B. Liu, D. Chen and G. Z. Shen. *Nanoscale*, 2012，**4**，3350.

40　J. Halme, P. Vahermaa, K. Miettunen, and P. Lund. *Adv. Mater*. 2010, **22**, E210.

41　J. Halme, G. Boschloo, A. Hagfeldt, and P. Lund. *J. Phys. Chem. C.* 2008, **112**, 5623.

42　P. E. de Jongh and D. Vanma ekelbergh. *J. Phys. Chem. B*. 1997, **101**, 2716.

43　D. S. Zhang, T. Yoshida, T. Oekermann, K. Furuta, and H. Minoura. *Adv. Funct. Mater.* 2006, **16**, 1228.

44　J. Kröger, R. Plass, M. Grätzel, P. J. Cameron, and L. M. Peter. *J. Phys. Chem. B.* 2003, **107**, 7536.

45　K. Zhu, N. R. Neal, A. Miedaner, and A. J. Frank. *Nano Lett.*, 2007, **7**, 69.

46　K. D. Benkstein, N. Kopidakis, J. van de Lagemaat, and A.J. Frank. *J. Phys. Chem. B*. 2003, **107**, 7759.

47　J. van de Lagemaat and A. J. Frank. *J. Phys. Chem. B.* 2001，**105**，11194.